

# Ferroelectric quantum critical point in superconducting hydrides: The case of H<sub>3</sub>S

Marco Cherubini,<sup>1,\*</sup> Abhishek Raghav,<sup>1,2</sup> and Michele Casula<sup>1,†</sup>

<sup>1</sup>*Institut de Minéralogie, de Physique des Matériaux et de Cosmochimie, CNRS, Sorbonne Université, 4 Place Jussieu, Paris, 75005, France*

<sup>2</sup>*RIKEN Center for Emergent Matter Science, 2-1 Hirosawa, Wako-shi, Saitama 351-0198, Japan*

(Dated: February 3, 2026)

H<sub>3</sub>S sulfur hydride has been widely investigated for its high superconducting critical temperature  $T_c$  of 203 K at about  $p_c = 155$  GPa. Despite being the precursor of superconducting hydrides, a detailed picture of its phase diagram in an extended temperature and pressure range is still missing. To determine it with inclusion of both thermal and quantum effects, we carry out path integral molecular dynamics combined to a MACE neural network potential trained on BLYP density functional theory configurations. The resulting H<sub>3</sub>S phase diagram is characterized by the ferroelectric transition between the Im $\bar{3}$ m and R3m phases, which originates from a quantum critical point (QCP) located at  $p_{QCP} \approx 134$  GPa. We show that the experimental  $T_c$  peak falls into a paraelectric region of large nuclear quantum fluctuations above the ferroelectric QCP, as measured by local phonon Green's functions resolved in imaginary time, where fluctuating dipole moments are at play. We study the critical behavior of the system in the proximity of the QCP by a finite-size scaling analysis, showing that it belongs to the 4D Ising universality class. We finally discuss its implications for the superconducting state.

Superconductivity was first discovered more than a century ago[1]. Since then, the quest for systems with high superconducting critical temperature ( $T_c$ ) has been one of the frontiers in both experimental and theoretical physics, with high values of  $T_c$  expected in systems containing light atoms[2, 3]. In 2015, a  $T_c$  of 203 K at about 150 GPa was measured in sulfur hydride (H<sub>3</sub>S)[4–8], exceeding the highest values found in cuprates[9–11]. In H<sub>3</sub>S, the superconducting critical temperature shows a dome-like shape as a function of pressure[4], similarly to what happens in cuprates[12, 13] or in certain dilute metals like SrTiO<sub>3</sub>[14–16]. The  $T_c$  peak at 155 GPa was originally associated with a ferroelectric phase transition[7] from the body-centered-cubic Im $\bar{3}$ m structure to the lower-symmetry trigonal R3m phase[17–19], triggered by the hydrogen (H) atoms displaced from their midpoint position between two flanking sulfur (S) atoms. However, theoretical attempts to study this transition failed to locate it at a pressure compatible with the position of the  $T_c$  peak, the most reliable theories placing the transition pressure more than 40 GPa below[20–22]. Nevertheless, a detailed picture of the H<sub>3</sub>S phase diagram is still missing, particularly its temperature evolution, which remains largely unexplored.

In this Letter, we fill this gap by studying the system over a large temperature and pressure range and by analyzing its quantum criticality in the proximity of the ferroelectric transition. By path integral molecular dynamics calculations (PIMD) with machine learning interatomic potential (MLIP) trained on density functional theory (DFT-BLYP)[23, 24], we unveil the presence of a ferroelectric quantum critical point (QCP) at  $134 \pm 2$  GPa belonging to the 4D Ising universality class (Fig. 1). According to our picture, the dome shape of the  $T_c$  evolution has a peak falling in the paraelectric Im $\bar{3}$ m phase,

and it is located in a region of strong quantum fluctuations surrounding the QCP, with superconductivity possibly enhanced by them.

In systems containing light atoms, like H<sub>3</sub>S, nuclear quantum fluctuations play a pivotal role. In this work, we use the PIMD formalism to treat nuclear quantum effects (NQE) exactly. However, its computational cost increases significantly as the temperature is lowered. Therefore, the combination of PIMD with *ab initio* elec-

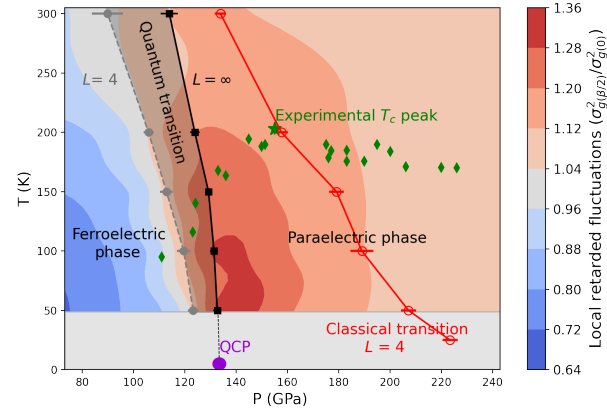


Figure 1. H<sub>3</sub>S phase diagram, computed by PIMD using a MACE-MLIP trained with a DFT-BLYP dataset for  $L = 4$ : ferroelectric transition (gray points, dashed line); classical molecular dynamics (MD) transition (red empty circles, solid line); extrapolated QCP (filled purple circle) and ferroelectric line (black squares, solid line); experimental superconducting  $T_c$  (green diamonds)[4, 5]. The colormap refers to the  $\sigma_{g(\beta/2)}^2/\sigma_{g(0)}^2$  ratio plotted in Fig. 2(d); it measures the relative intensity of the retarded fluctuations of local moments. Data are interpolated using a weighted sum of radially symmetric basis functions. Blue and red shaded areas are the ferroelectric and paraelectric phases, respectively.

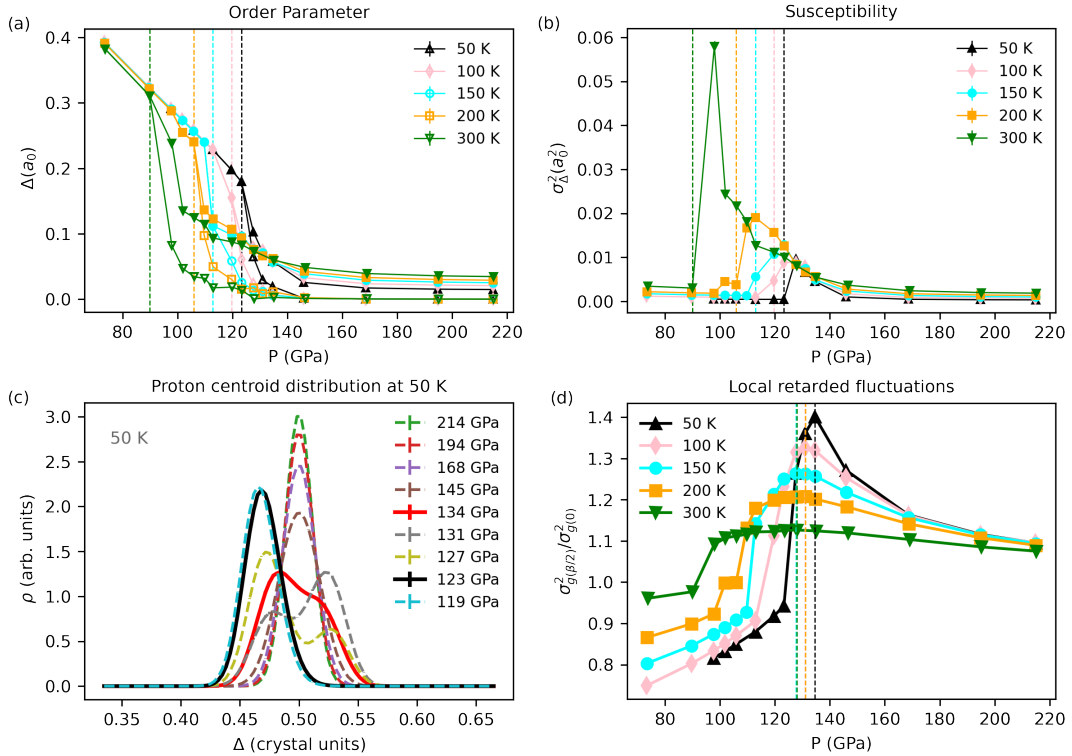


Figure 2. Order parameter and local observables for  $L = 4$ . Panel (a): Order parameter for the ferroelectric transition. Full and empty symbols are the absolute and the real values of the order parameter,  $\Delta_{\text{abs}}$  and  $\Delta$ , respectively. The variance of  $\Delta$  is in panel (b). Different temperatures are reported: 50 K (black triangles), 100 K (pink diamonds), 150 K (cyan circles), 200 K (orange squares) and 300 K (green reversed triangles). The vertical dashed lines indicate the transition pressures. Panel (c): Proton centroids distribution along the S-S direction for several pressures at  $T = 50$  K. Thick black and red curves indicate the ferroelectric transition and the unimodal-to-bimodal variation, respectively. Panel (d):  $\sigma_{g(\beta/2)}/\sigma_{g(0)}$  ratio, where  $\sigma_{g(\tau)}$  is the variance of the local Green function in imaginary time. Dashed lines indicate its maximum.

tronic structure methods, such as DFT, to explore the full phase diagram of sulfur hydride is unfeasible. Here, to maintain the DFT-level accuracy at a much lower computational cost, we trained a MLIP using MACE[25, 26]. Then, we ran NVT-PIMD simulations at different volumes  $V$  and temperatures  $T = 1/(k_B\beta)$ , using the i-PI package[27] in combination with the generated MLIP. Quantum nuclei are necklaces made of  $L_\tau$  beads, such that  $\beta = L_\tau \delta\tau$ , with  $\delta\tau$  the imaginary time step assuring convergence. The simulations are up to 400 ps long, for systems made of  $L \times L \times L$  primitive cells with  $L \in \{2, 3, 4\}$ , necessary for an accurate determination of phase boundaries via finite-size scaling. Further details about the PIMD simulations and the MLIP generation can be found in the Supplemental Material (SM)[28].

The ferroelectric  $\bar{I}m\bar{3}m$  and paraelectric  $R\bar{3}m$  structures differ by the average protons position with respect to their neighboring S atoms. To distinguish the two symmetries, we define the global proton displacement

$$\Delta^{(j)} = \frac{1}{N_H} \sum_{i=1}^{N_H} [\vec{r}_{H_i S_{i_1}}^{(j)} \cdot \hat{r}_{S_{i_1} S_{i_2}}^{(j)} - d_{S_{i_1} S_{i_2}}^{(j)}/2], \quad (1)$$

evaluated at the  $j$ -th PIMD iteration. For every hydrogen atom  $H_i$  in the supercell, we identify its two flanking S atoms,  $S_{i_1}$  and  $S_{i_2}$ . Then, we project the vector  $\vec{r}_{H_i S_{i_1}}$ , connecting  $H_i$  to one of the two S atoms, onto the  $S_{i_1}$ - $S_{i_2}$  direction. Finally, the distance between the projection and the  $S_{i_1}$ - $S_{i_2}$  midpoint is summed over the  $N_H$  hydrogen atoms in the supercell.  $H_i$ ,  $S_{i_1}$  and  $S_{i_2}$  are taken here as centroid positions. Equivalent results can be obtained for bead positions (see SM[28]). To appropriately define a scalar order parameter for the ferroelectric transition, we establish a reference for the positive direction of these displacements. To do so, we project them onto the eight different degenerate orientations that the  $H_3S$  molecule can assume in sulfur hydride, and we take the one that maximizes the order parameter  $\Delta$ , defined as the average of the global displacements over the entire PIMD trajectory made of  $N$  steps, i.e.,  $\Delta = \frac{1}{N} \sum_{j=1}^N \Delta^{(j)}$ . For this orientation, we compute also  $\Delta_{\text{abs}} = \frac{1}{N} \sum_{j=1}^N |\Delta^{(j)}|$ . All global displacements  $\Delta^{(j)}$  belonging to the same PIMD trajectory are computed with respect to the same reference orientation.

To better identify the ferroelectric transition, we ex-

ploit a combined analysis of  $\Delta$  and  $\Delta_{\text{abs}}$  (Fig. 2(a)). At the transition, the protons freeze in one of the degenerate minima of the underlying potential energy surface (PES). When this happens, the order parameter  $\Delta$  and its absolute value  $\Delta_{\text{abs}}$  become indistinguishable, because the fluctuations are suppressed. Simultaneously, the variance of the order parameter,  $\sigma_{\Delta}^2$ , suddenly drops (Fig. 2(b)). By employing these two criteria, i.e. order parameter saturation and frozen fluctuations, we unambiguously identify the ferroelectric transition line as a function of temperature (Fig. 1). The critical pressure increases as the temperature is lowered, with a pressure-versus-temperature slope that decreases upon cooling the system. A ferroelectric quantum critical point (QCP) emerges at  $T = 0$  K, where the transition is purely driven by quantum fluctuations. Here, the PIMD formalism cannot be used to describe the system. However, we can identify the location of the QCP at  $p_{\text{QCP}} \approx 134 \pm 2$  GPa by extrapolating in temperature and size.

To further characterize the  $\text{H}_3\text{S}$  ferroelectric transition, we can also look at the local proton displacement, or local dipole moment

$$\Delta_i^{(j)} = \hat{r}_{\text{H}_i \text{S}_{i_1}}^{(j)} \cdot \hat{r}_{\text{S}_{i_1} \text{S}_{i_2}}^{(j)} - d_{\text{S}_{i_1} \text{S}_{i_2}}^{(j)} / 2, \quad (2)$$

defined for the centroid coordinates, as in Eq. 1. Its distribution, gathered for all atoms  $H_i$  and PIMD iterations, is shown in Fig. 2(c) for  $T = 50$  K and different pressures. In a scenario characterized by a displacive transition, the H atoms display very different behaviors according to the underlying PES shape. Deep in the paraelectric phase, at very high pressures, the potential exhibits a single well and the H atoms stay on average at the S-S segment midpoint, resulting in a unimodal symmetric distribution. Upon decompression, the potential acquires a displaced global minimum which is eight-fold degenerate. In the distribution of the local parameter  $\Delta_i^{(j)}$ , this is reflected in the development of a bimodal shape, or peak-split density, whose lobes correspond to the positive and negative  $H_i$  projections along the corresponding  $\text{S}_{i_1}$ - $\text{S}_{i_2}$  direction. It is the regime of pre-formed local dipole moments, fluctuating across a central barrier. This corresponds to increased fluctuations of the order parameter, detected by  $\sigma_{\Delta}^2$  (Fig. 2(b)), while  $\Delta$  is still zero on average. Upon further decompression, the potential barrier increases to the point where protons can no longer cross it, freezing in one of the degenerate minima; the distribution of the local proton displacement returns unimodal but shifted from the S-S midpoint. This leads to the creation of a permanent local dipole moment, generated by the displaced protons in the R3m phase. Interestingly, although  $\Delta_i^{(j)}$  is a local property, it can be used as an additional probe for the ferroelectric transition, because in  $\text{H}_3\text{S}$  the local moments, once frozen, are long-range ordered. The other temperatures show the same phenomenology: by reducing the pressure, we ob-

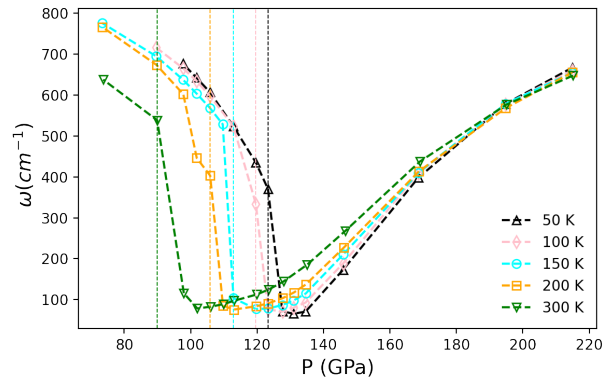


Figure 3. Soft optical mode frequencies as a function of pressure at different temperatures computed for  $L = 4$  from PIMD phonons[29] (see also the SM[28]). Colors and symbols are the same as Fig. 2(a)-(b). Dashed vertical lines indicate the ferroelectric transition.

serve first a crossover from unimodal to bimodal  $\Delta_i^{(j)}$  distributions with zero order parameter  $\Delta$ , and then an off-centered unimodal shape at the ferroelectric transition (see SM[28]). The density peak splitting associated with the local moment formation does not show a significant temperature dependence. The ferroelectric transition line approaches the local moment formation pressures only at the lowest temperatures, owing to reduced thermal fluctuations. At  $T = 200$  K the ferroelectric critical pressure is  $124 \pm 2$  GPa, significantly lower than the experimental  $T_c$  peak located at about 155 GPa. This mismatch is aligned with other theoretical predictions [21, 22]. Moreover, a comparison with classical MD results, also reported in Fig. 1, shows that the ferroelectric transition pressure is strongly reduced by NQE ( $\approx 50$  GPa shift from the classical value at  $T = 200$  K).

One of the properties most sensitive to structural transitions is lattice dynamics, encoded by the imaginary-time phonon Green function:

$$G_{x_i, x_j}(\tau) = -\sqrt{m_i m_j} \langle \mathcal{T} \delta x_i(\tau) \delta x_j(0) \rangle, \quad (3)$$

with  $m_i$  the mass of the  $i$ -th atom,  $\mathcal{T}$  the time-ordered operator and  $\delta x_i(\tau)$  the displacement operator evaluated at the imaginary time  $\tau$  along the direction  $x$ . The quantum correlator  $\langle \delta x_i(\tau) \delta x_j(0) \rangle$  is accessible by PIMD, where the atomic displacement,  $\delta x_i(\tau) = x_i(\tau) - \langle x_i \rangle$ , is defined with respect to  $\langle x_i \rangle$ , the quantum thermal average of the coordinate  $x_i$ , and evaluated on the  $L_\tau$  points in the imaginary time interval  $[0, \beta]$ . Within PIMC, one can easily compute the Kubo-transformed version of Eq. 3, which corresponds to the static limit of the Matsubara Green function[29]. Diagonalizing its inverse yields the anharmonic phonons frequencies in the static approximation[29, 30]. Dispersive phonon branches are obtained by Fourier transforming the spatial coordinates  $x$ . In Fig. 3, we focus on the optical phonons at the

$\Gamma$  point that correspond to the modes driving the ferroelectric transition. Their patterns are a combination of H shuttling modes along the S-S direction and S-H-S bending modes, leading to the formation of distinct  $\text{H}_3\text{S}$  molecules in the crystal. A phonon softening is apparent when approaching the transition from the paraelectric phase, while a sharp jump takes place at the transition. The phonon softening is related to a vanishing curvature of the PES; the sharp frequency increase is due to a stiffer potential experienced by protons once frozen in the ferroelectric configuration. Note how at each temperature the frequency jump happens exactly at the corresponding critical pressure, as detected from  $\Delta$  and its variance  $\sigma_\Delta^2$ . This is the typical picture of a second-order phase transition, which goes through a sign change of the PES curvature. The softening of these modes has already been associated to the ferroelectric transition[21, 22]. However, we provide here an unprecedented resolution of their temperature dependence, thanks to the MLIP acceleration and a larger statistics.

We characterize the universality class of the transition at the QCP by performing a finite-size scaling analysis. Close to a QCP, observables  $\mathcal{O}$  are expected to scale as [31–33]

$$\mathcal{O} = L^{-x_\mathcal{O}} \tilde{\mathcal{O}}(uL^{1/\nu}, L_\tau/L^z), \quad (4)$$

where  $u = \frac{V-V_c}{V_c}$  is the reduced coupling, with  $V_c$  the critical volume, and  $x_\mathcal{O}$  the scaling dimension of the observable  $\mathcal{O}$ .  $\nu$  is the correlation length exponent, while the dynamical critical exponent  $z$  governs the temperature dependence. When applying Eq. 4 to the order parameter, i.e.  $\mathcal{O} = \Delta$ , we assume Lorentz invariance ( $z = 1$ ) and vanishing anomalous dimension ( $x_\Delta = 1$ ), fulfilled by the Ising universality class[31, 34]. In fact, the computed grid of temperatures and supercell sizes, limited by the expensive cost of PIMD simulations, prevents the direct determination of  $z$  from our data. Therefore, we assume the validity of the Ising universality class and, in order to check whether our data are compatible with this scenario, we focus on the critical exponent  $\nu$ . Given  $z = 1$ , we fix the  $L_\tau/L$  ratio to be a constant, such that the scaling function in Eq. 4 depends only on one variable. Thus, the scaling analysis is performed using simulations at  $T = 50$  K ( $L_\tau = 100$ ,  $L = 4$ ), 67 K ( $L_\tau = 75$ ,  $L = 3$ ), and 100 K ( $L_\tau = 50$ ,  $L = 2$ ) for different volumes. To obtain  $\nu$ , we look for the value that makes  $L\Delta$  best collapse onto a unique curve (Fig. 4). We identify it by minimizing the cost function  $C(\nu) = \sum_j |y_{j+1} - y_j| / (\max(y_j) - \min(y_j)) - 1$ , where  $y_j$  are the values of the order parameter for all temperatures, volumes and sizes, ordered according to the  $uL^{1/\nu}$  product[33, 35, 36]. We found that the optimal value is  $\nu \sim 0.483 \pm 0.014$  (see inset of Fig. 4), consistent with the 4D Ising universality class ( $\nu = \frac{1}{2}$ ). Accordingly, we accurately extrapolated the ferroelectric transition line to the thermodynamic limit, by including the logarithmic

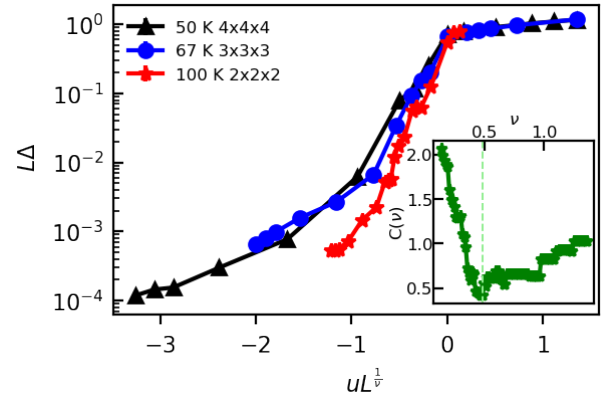


Figure 4. Finite-size scaling of  $\Delta$  at  $T = 50$  K (black triangles), 67 K (blue circles) and 100 K (red stars), and supercell sizes chosen to keep  $L_\tau/L$  constant. We use  $g[uL^{1/\nu}]$  as a functional form, where  $u = \frac{V-V_c}{V_c}$ , with  $V_c$  the critical volume. Inset: the critical exponent  $\nu$  is obtained by minimizing the cost function  $C(\nu)$  defined in the text.

corrections appearing at the upper critical dimension[37–39], such that  $p_{\text{QCP}}(L) = p_{\text{QCP}}(\infty) + \alpha L^{-2} \ln(L)^{-1/6}$  at fixed temperature (Fig. 1 and SM[28]).

Having established the accurate location of the  $\text{H}_3\text{S}$  ferroelectric transition and its 4D Ising universality class, we then quantify the magnitude of quantum fluctuations across the transition. This information is encoded in the imaginary time evolution, accessible in PIMD. Given the importance of the shuttling modes (Fig. 3) in driving the transition, it is worth studying the full time dependence of the phonon Green function projected on the proton local displacements (Eq. 2),  $g(\tau) \equiv G_{ii}(\tau)$ , where  $i$  is the H atom index. We thus extended the approach of Ref. [29] in order to compute the displacement-displacement correlators in Eq. 3 by fully retaining their imaginary time dependence. In the case of a local moment formation,  $g(\beta/2)$  saturates to a finite value, due to the freezing of local quantum fluctuations, while in absence of preformed local moments  $g(\beta/2) \propto \exp(-k\beta) \simeq 0$ . Therefore, the variance of  $g(\beta/2)$ , i.e.  $\sigma_{g(\beta/2)}^2$ , bears information on the formation of stable local moments. More specifically, we compute the normalized variance  $\sigma_{g(\beta/2)}^2 / \sigma_{g(0)}^2$ , in order to isolate the contribution of retardation effects at  $\tau = \beta/2$  from the instantaneous moments formation at  $\tau = 0$ . Fig. 2(d) shows the pressure dependence of  $\sigma_{g(\beta/2)}^2 / \sigma_{g(0)}^2$  for all temperatures studied. Its maximum at  $T = 50$  K matches the pressures where the unimodal-to-bimodal variation occurs in the local density (Fig. 2(c)), while the  $\sigma_{g(\beta/2)}^2 / \sigma_{g(0)}^2$  ratio decreases sharply in the ferroelectric phase, when the H atoms freeze into one of the displaced minima, where fluctuations are strongly suppressed. At higher temperatures, the  $\sigma_{g(\beta/2)}^2 / \sigma_{g(0)}^2$  peak is shallower but still well defined, indicating that retardation effects are still relevant, although weaker. Its location is nearly

temperature-independent. To have a more comprehensive view of the retardation effects, in Fig. 1 we plot  $\sigma_{g(\beta/2)}^2/\sigma_{g(0)}^2$  as a heatmap in the  $(p, T)$  plane. It shows how the ferroelectric phase is characterized by suppressed quantum fluctuations. On the other hand, large fluctuations, only marginally irrelevant in 4D, are present in the paraelectric side, stretching over a wide  $(p, T)$  domain.

It is intriguing that the experimental superconducting  $T_c$  peak is quite far from the ferroelectric transition line, while falling in a paraelectric region with strong retardation effects spawned by the QCP. It is already known that NQE can enhance the superconducting critical temperature of a BCS superconductor, as shown in the atomic phase of pristine hydrogen[40]. This requires going beyond the standard Migdal-Eliashberg framework[41] by taking into account phonon renormalization effects[42, 43] through the inclusion of the full frequency dependence of the phonon Green function, beside the multi-band and the  $k$ -dependence nature of the electron-phonon interaction[44, 45], and its vertex corrections[46–48]. In the case of  $H_3S$ , source of these effects is the proximity of the ferroelectric QCP, which then calls for a more appropriate evaluation of the superconducting  $T_c$  in this material. At the same time, it would be desirable to estimate the electron-phonon coupling within a non-perturbative framework, such as the one proposed in Ref. [49]. Indeed, the presence of a ferroelectric QCP has been invoked to explain the enhancement of superconductivity in some dilute metals like  $SrTiO_3$  [14–16, 50–52], by relying on an electron-pairing mechanism beyond linear order in the electron-phonon vertex, namely mediated by two optical phonons[14]. Although it remains to verify whether  $H_3S$  meets similar conditions, the application of the latter picture to this material is tempting, owing to the presence of optical phonons with strong spectral weight[53], significantly softened at the ferroelectric transition (Fig. 3), and to the strong renormalization of both one-body and two-body phonon Green functions (Fig. 1 and SM[28]).

To conclude, we have characterized the phase diagram of  $H_3S$  over a wide range of pressures and temperatures, by unveiling the 4D Ising universality class of its ferroelectric quantum criticality, the location of the QCP and its transition line from BLYP-MLIP driven PIMD. The emerging scenario for the high- $T_c$  superconductivity in  $H_3S$  appears more complex than previously thought. Indeed, according to our calculations the maximum of the superconducting  $T_c$  falls in a paraelectric region dominated by quantum fluctuations and retardation effects surrounding the QCP, which could both affect superconductivity.

*Acknowledgments* - We acknowledge GENCI for providing computational resources on the IDRIS Jean-Zay supercomputing clusters and TGCC Joliot-Curie Rome partition under project number A0170906493. We are grateful for computational resources from EuroHPC for

the computational grant EHPC-EXT-2024E01-064 allocated on Leonardo (booster partition). We acknowledge EPICURE, a EuroHPC Joint Undertaking initiative for supporting this project on the booster partition of Leonardo through the EuroHPC JU 2024E01 call for proposals for extreme scale access mode. We thank the European High Performance Computing Joint Undertaking (JU) for the support through the "EU-Japan Alliance in HPC" HANAMI project (Hpc AlliaNce for Applications and supercoMputing Innovation: the Europe - Japan collaboration). A.R. acknowledges financial support from JST BOOST (Grant No. JPMJBY24F3). We thank Pr. Ryotaro Arita, Pr. Matteo Calandra, Dr. Lorenzo Monacelli, Dr. Tommaso Morresi, and Dr. Kosuke Nakano for useful discussions.

*Data availability* - The data that support the findings of this article are openly available at [54].

---

\* marco.cherubini@sorbonne-universite.fr

† michele.casula@sorbonne-universite.fr

- [1] H. Onnes, The Superconductivity of Mercury, *Comm. Phys. Lab. Univ.*, Leiden , 122 (1911).
- [2] N. W. Ashcroft, Metallic Hydrogen: A High-Temperature Superconductor?, *Physical Review Letters* **21**, 1748–1749 (1968).
- [3] L. P. Gor'kov and V. Z. Kresin, Pressure and high-T<sub>c</sub> superconductivity in sulfur hydrides, *Scientific Reports* **6**, 10.1038/srep25608 (2016).
- [4] A. P. Drozdov, M. I. Eremets, I. A. Troyan, V. Ksenofontov, and S. I. Shylin, Conventional superconductivity at 203 kelvin at high pressures in the sulfur hydride system, *Nature* **525**, 73 (2015).
- [5] M. Einaga, M. Sakata, T. Ishikawa, K. Shimizu, M. I. Eremets, A. P. Drozdov, I. A. Troyan, N. Hirao, and Y. Ohishi, Crystal structure of the superconducting phase of sulfur hydride, *Nature Physics* **12**, 835 (2016).
- [6] S. Mozaffari, D. Sun, V. S. Minkov, A. P. Drozdov, D. Knyazev, J. B. Betts, M. Einaga, K. Shimizu, M. I. Eremets, L. Balicas, and F. F. Balakirev, Superconducting phase diagram of  $H_3S$  under high magnetic fields, *Nature Communications* **10**, 2522 (2019).
- [7] V. S. Minkov, V. B. Prakapenka, E. Greenberg, and M. I. Eremets, A Boosted Critical Temperature of 166 K in Superconducting  $D_3S$  Synthesized from Elemental Sulfur and Hydrogen, *Angewandte Chemie International Edition* **59**, 18970 (2020).
- [8] I. Osmond, O. Moulding, S. Cross, T. Muramatsu, A. Brooks, O. Lord, T. Fedotenko, J. Buhot, and S. Friedemann, Clean-limit superconductivity in  $Im\bar{3}m$   $H_3S$  synthesized from sulfur and hydrogen donor ammonia borane, *Phys. Rev. B* **105**, L220502 (2022).
- [9] J. G. Bednorz and K. A. Muller, Possible high  $t_c$  superconductivity in the Ba-La-Cu-O system, *Zeitschrift fur Physik B Condensed Matter* **64**, 189–193 (1986).
- [10] L. Gao, Y. Y. Xue, F. Chen, Q. Xiong, R. L. Meng, D. Ramirez, C. W. Chu, J. H. Eggert, and H. K. Mao, Superconductivity up to 164 K in  $HgBa_2Ca_{m-1}Cu_mO_{2m+2+\delta}$  (m=1, 2, and 3) un-

- der quasihydrostatic pressures, *Physical Review B* **50**, 4260–4263 (1994).
- [11] A. Bianconi and T. Jarlborg, Superconductivity above the lowest earth temperature in pressurized sulfur hydride, *EPL (Europhysics Letters)* **112**, 37001 (2015).
- [12] B. Keimer, S. A. Kivelson, M. R. Norman, S. Uchida, and J. Zaanen, From quantum matter to high-temperature superconductivity in copper oxides, *Nature* **518**, 179 (2015).
- [13] B. Michon, C. Girod, S. Badoux, J. Kačmarčík, Q. Ma, M. Dragomir, H. Dabkowska, B. Gaulin, J.-S. Zhou, S. Pyon, *et al.*, Thermodynamic signatures of quantum criticality in cuprate superconductors, *Nature* **567**, 218 (2019).
- [14] K. L. Ngai, Two-Phonon Deformation Potential and Superconductivity in Degenerate Semiconductors, *Physical Review Letters* **32**, 215–218 (1974).
- [15] D. E. Kiselov and M. V. Feigel'man, Theory of superconductivity due to Ngai's mechanism in lightly doped  $\text{SrTiO}_3$ , *Physical Review B* **104**, 10.1103/physrevb.104.l220506 (2021).
- [16] D. van der Marel, F. Barantani, and C. W. Rischau, Possible mechanism for superconductivity in doped  $\text{SrTiO}_3$ , *Physical Review Research* **1**, 10.1103/physrevresearch.1.013003 (2019).
- [17] D. Duan, Y. Liu, F. Tian, D. Li, X. Huang, Z. Zhao, H. Yu, B. Liu, W. Tian, and T. Cui, Pressure-induced metallization of dense  $(\text{H}_2\text{S})_2\text{H}_2$  with high- $T_c$  superconductivity, *Scientific reports* **4**, 6968 (2014).
- [18] J. A. Flores-Livas, A. Sanna, and E. Gross, High temperature superconductivity in sulfur and selenium hydrides at high pressure, *The European Physical Journal B* **89**, 63 (2016).
- [19] A. F. Goncharov, S. S. Lobanov, V. B. Prakapenka, and E. Greenberg, Stable high-pressure phases in the H-S system determined by chemically reacting hydrogen and sulfur, *Phys. Rev. B* **95**, 140101 (2017).
- [20] I. Errea, M. Calandra, C. J. Pickard, J. R. Nelson, R. J. Needs, Y. Li, H. Liu, Y. Zhang, Y. Ma, and F. Mauri, Quantum hydrogen-bond symmetrization in the superconducting hydrogen sulfide system, *Nature* **532**, 81 (2016).
- [21] R. Bianco, I. Errea, M. Calandra, and F. Mauri, High-pressure phase diagram of hydrogen and deuterium sulfides from first principles: Structural and vibrational properties including quantum and anharmonic effects, *Phys. Rev. B* **97**, 214101 (2018).
- [22] R. Taureau, M. Cherubini, T. Morresi, and M. Casula, Quantum symmetrization transition in superconducting sulfur hydride from quantum Monte Carlo and path integral molecular dynamics, *npj Computational Materials* **10**, 10.1038/s41524-024-01239-0 (2024).
- [23] A. D. Becke, Density-functional exchange-energy approximation with correct asymptotic behavior, *Phys. Rev. A* **38**, 3098 (1988).
- [24] C. Lee, W. Yang, and R. G. Parr, Development of the Colle-Salvetti correlation-energy formula into a functional of the electron density, *Physical review B* **37**, 785 (1988).
- [25] I. Batatia, D. P. Kovacs, G. N. C. Simm, C. Ortner, and G. Csanyi, MACE: Higher Order Equivariant Message Passing Neural Networks for Fast and Accurate Force Fields, in *Advances in Neural Information Processing Systems*, edited by A. H. Oh, A. Agarwal, D. Belgrave, and K. Cho (2022).
- [26] I. Batatia, S. Batzner, D. P. Kovács, A. Musaelian, G. N. C. Simm, R. Drautz, C. Ortner, B. Kozinsky, and G. Csányi, The Design Space of  $E(3)$ -Equivariant Atom-Centered Interatomic Potentials (2022), arXiv:2205.06643.
- [27] M. Ceriotti, J. More, and D. E. Manolopoulos, i-PI: A Python interface for ab initio path integral molecular dynamics simulations, *Computer Physics Communications* **185**, 1019–1026 (2014).
- [28] See Supplemental Material at [URL will be inserted by publisher] for additional information about the computational details of PIMD and classical MD simulations, the MLIP training and validation, the bead-resolved and imaginary-time resolved estimators, and the 2-body Green function calculations (see references [4, 5, 15, 21–27, 29, 30, 37–39, 55–59] therein).
- [29] T. Morresi, L. Paulatto, R. Vuilleumier, and M. Casula, Probing anharmonic phonons by quantum correlators: A path integral approach, *The Journal of Chemical Physics* **154**, 224108 (2021).
- [30] T. Morresi, R. Vuilleumier, and M. Casula, Hydrogen phase-IV characterization by full account of quantum anharmonicity, *Physical Review B* **106**, 054109 (2022).
- [31] S. Sachdev, *Quantum Phase Transitions* (Cambridge University Press, 2011).
- [32] D.-H. Kim, Y.-C. Lin, and H. Rieger, Path integral Monte Carlo study of the interacting quantum double-well model: Quantum phase transition and phase diagram, *Physical Review E* **75**, 10.1103/physreve.75.016702 (2007).
- [33] R. Mondaini, S. Tarat, and R. T. Scalettar, Universality and critical exponents of the fermion sign problem, *Physical Review B* **107**, 10.1103/physrevb.107.245144 (2023).
- [34] F. F. Assaad and I. F. Herbut, Pinning the Order: The Nature of Quantum Criticality in the Hubbard Model on Honeycomb Lattice, *Physical Review X* **3**, 031010 (2013).
- [35] J. Šuntajs, J. Bonča, T. Prosen, and L. Vidmar, Ergodicity breaking transition in finite disordered spin chains, *Physical Review B* **102**, 064207 (2020).
- [36] A. S. Aramthottil, T. Chanda, P. Sierant, and J. Zakrzewski, Finite-size scaling analysis of the many-body localization transition in quasiperiodic spin chains, *Phys. Rev. B* **104**, 214201 (2021).
- [37] E. Brézin, An investigation of finite size scaling, *Journal de Physique* **43**, 15 (1982).
- [38] N. Aktekin, The finite-size scaling functions of the four-dimensional Ising model, *Journal of Statistical Physics* **104**, 1397 (2001).
- [39] R. Kenna, Finite size scaling for  $O(N)$   $\varphi 4$ -theory at the upper critical dimension, *Nuclear Physics B* **691**, 292 (2004).
- [40] Đ. Dangić, L. Monacelli, R. Bianco, F. Mauri, and I. Errea, Large impact of phonon lineshapes on the superconductivity of solid hydrogen, *Communications Physics* **7**, 150 (2024).
- [41] F. Marsiglio, Eliashberg theory: A short review, *Annals of Physics* **417**, 168102 (2020).
- [42] F. Marsiglio, Phonon Self-Energy Effects in Migdal-Eliashberg Theory, in *Electron-Phonon Interaction in Oxide Superconductors*, edited by R. Baquero (World Scientific, Singapore, 1991) p. 167.
- [43] I. Esterlis, B. Nosarzewski, E. W. Huang, B. Moritz, T. P. Devereaux, D. J. Scalapino, and S. A. Kivelson,

- Breakdown of the Migdal-Eliashberg theory: A determinant quantum Monte Carlo study, *Physical Review B* **97**, 140501 (2018).
- [44] W. Sano, T. Koretsune, T. Tadano, R. Akashi, and R. Arita, Effect of Van Hove singularities on high- $T_c$  superconductivity in  $H_3S$ , *Physical Review B* **93**, 094525 (2016).
- [45] R. Lucrezi, P. P. Ferreira, S. Hajinazar, H. Mori, H. Paudyal, E. R. Margine, and C. Heil, Full-bandwidth anisotropic Migdal-Eliashberg theory and its application to superhydrides, *Communications Physics* **7**, 33 (2024).
- [46] L. Pietronero, S. Strässler, and C. Grimaldi, Nonadiabatic superconductivity. I. Vertex corrections for the electron-phonon interactions, *Physical Review B* **52**, 10516 (1995).
- [47] C. Grimaldi, L. Pietronero, and S. Strässler, Nonadiabatic superconductivity. II. Generalized Eliashberg equations beyond Migdal's theorem, *Physical Review B* **52**, 10530 (1995).
- [48] S. B. Mishra, H. Mori, and E. R. Margine, Electron-phonon vertex correction effect in superconducting  $h_3s$ , *npj Computational Materials* **11**, 342 (2025).
- [49] R. Bianco and I. Errea, Non-perturbative theory of the electron-phonon coupling and its first-principles implementation, *arXiv preprint arXiv:2303.02621* (2023).
- [50] C. Collignon, X. Lin, C. W. Rischau, B. Fauqué, and K. Behnia, Metallicity and superconductivity in doped strontium titanate, *Annual Review of Condensed Matter Physics* **10**, 25 (2019).
- [51] M. N. Gastiasoro, J. Ruhman, and R. M. Fernandes, Superconductivity in dilute  $SrTiO_3$ : A review, *Annals of Physics* **417**, 168107 (2020).
- [52] P. A. Volkov, P. Chandra, and P. Coleman, Superconductivity from energy fluctuations in dilute quantum critical polar metals, *Nature communications* **13**, 4599 (2022).
- [53] F. Capitani, B. Langerome, J.-B. Brubach, P. Roy, A. Drozdov, M. Eremets, E. Nicol, J. Carbotte, and T. Timusk, Spectroscopic evidence of a new energy scale for superconductivity in  $H_3S$ , *Nature physics* **13**, 859 (2017).
- [54] M. Cherubini, A. Raghav, and M. Casula, Additional data for "Ferroelectric quantum critical point in superconducting hydrides: The case of  $H_3S$ " (2026).
- [55] M. Ceriotti, M. Parrinello, T. E. Markland, and D. E. Manolopoulos, Efficient stochastic thermostatting of path integral molecular dynamics, *The Journal of Chemical Physics* **133**, 10.1063/1.3489925 (2010).
- [56] P. Giannozzi, S. Baroni, N. Bonini, M. Calandra, R. Car, C. Cavazzoni, D. Ceresoli, G. L. Chiarotti, M. Cococcioni, I. Dabo, A. Dal Corso, S. de Gironcoli, S. Fabris, G. Fratesi, R. Gebauer, U. Gerstmann, C. Goucoussis, A. Kokalj, M. Lazzeri, L. Martin-Samos, N. Marzari, F. Mauri, R. Mazzarello, S. Paolini, A. Pasquarello, L. Paulatto, C. Sbraccia, S. Scandolo, G. Sclauzero, A. P. Seitsonen, A. Smogunov, P. Umari, and R. M. Wentzcovitch, QUANTUM ESPRESSO: a modular and open-source software project for quantum simulations of materials, *Journal of Physics: Condensed Matter* **21**, 395502 (2009).
- [57] P. Giannozzi, O. Andreussi, T. Brumme, O. Bunau, M. Buongiorno Nardelli, M. Calandra, R. Car, C. Cavazzoni, D. Ceresoli, M. Cococcioni, N. Colonna, I. Carnimeo, A. Dal Corso, S. de Gironcoli, P. Delugas, R. A. DiStasio, A. Ferretti, A. Floris, G. Fratesi, G. Fugallo, R. Gebauer, U. Gerstmann, F. Giustino, T. Gorni, J. Jia, M. Kawamura, H.-Y. Ko, A. Kokalj, E. Küçükbenli, M. Lazzeri, M. Marsili, N. Marzari, F. Mauri, N. L. Nguyen, H.-V. Nguyen, A. Otero-de-la Roza, L. Paulatto, S. Ponc  , D. Rocca, R. Sabatini, B. Santra, M. Schlipf, A. P. Seitsonen, A. Smogunov, I. Timrov, T. Thonhauser, P. Umari, N. Vast, X. Wu, and S. Baroni, Advanced capabilities for materials modelling with Quantum ESPRESSO, *Journal of Physics: Condensed Matter* **29**, 465901 (2017).
- [58] J. Gilmer, S. S. Schoenholz, P. F. Riley, O. Vinyals, and G. E. Dahl, Neural Message Passing for Quantum Chemistry, in *Proceedings of the 34th International Conference on Machine Learning*, Proceedings of Machine Learning Research, Vol. 70, edited by D. Precup and Y. W. Teh (PMLR, 2017) pp. 1263–1272.
- [59] M. M. Bronstein, J. Bruna, T. Cohen, and P. Veli  kovi  , Geometric Deep Learning: Grids, Groups, Graphs, Geodesics, and Gauges (2021).

## Supplemental Material: Ferroelectric quantum critical point in superconducting hydrides: The case of $H_3S$

Marco Cherubini,<sup>1,\*</sup> Abhishek Raghav,<sup>1,2</sup> and Michele Casula<sup>1,†</sup>

<sup>1</sup>*Institut de Minéralogie, de Physique des Matériaux et de Cosmochimie, CNRS, Sorbonne Université, 4 Place Jussieu, Paris, 75005, France*

<sup>2</sup>*RIKEN Center for Emergent Matter Science, 2-1 Hirosawa, Wako-shi, Saitama 351-0198, Japan*

(Dated: January 31, 2026)

### METHODS

We carried out path integral molecular dynamics (PIMD) simulations at various temperatures,  $T = 50$  K, 100 K, 150 K, 200 K and 300 K, using 100, 48, 32, 24 and 16 beads, respectively. The number of beads  $L_\tau$  employed for each temperature guarantees the convergence of the PIMD kinetic energy [1], by keeping the imaginary time step  $\delta\tau = \beta/L_\tau$  constant over the temperature grid, with  $\beta = 1/(k_B T)$ . The nuclei are evolved in time using the PILE integrator [2] within the i-Pi package [3]. A time step of 0.4 fs and a Langevin thermostat relaxation time of 50 fs are used. For classical molecular dynamics (MD), we performed simulations at the same temperatures with an additional simulation at  $T = 25$  K. Unfortunately, lower temperatures could not be explored due to ergodicity-breaking issues. We used a classical Langevin dynamic thermostat [2] with the same time step and thermostat relaxation time as in the PIMD simulations. Quantum simulations are approximately 40 - 50 ps long, except for those near the ferroelectric transition, where longer correlation times require simulations of the order of 200 - 400 ps to converge. On the other hand, all the classical trajectories are at least 400 ps long, thanks to their reduced computational cost. In principle, the  $Im\bar{3}m \rightarrow R3m$  transformation is also accompanied by a trigonal distortion of the lattice. However, denisty functional theory (DFT) calculations [4] report a very weak trigonal distortion ( $\leq 0.05^\circ$ ), confirmed by our *ab initio* calculations. Supported by this finding, we run PIMD-NVT simulations constraining the unit cell vectors to the  $Im\bar{3}m$  shape, and letting the sulfur (S) and hydrogen (H) atoms free to move in the supercell. The corresponding pressure with the quantum contribution included is directly provided by the i-PI engine.

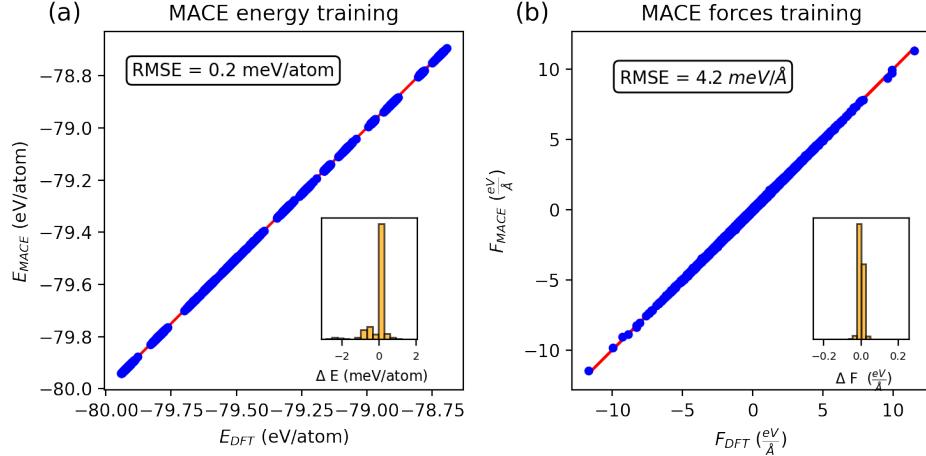


Figure 1. Evaluation of the MLIP on a 3660 configuration test set. Panel (a): Comparison between the energies predicted by the MACE model  $E_{MACE}$  and the DFT-BLYP reference energies  $E_{DFT}$ . Panel (b): forces predicted by the MACE model  $F_{MACE}$  compared with the DFT-BLYP references  $F_{DFT}$ . In both panels, the red line indicates the perfect correspondence. The histograms in the insets both panels show the corresponding error distributions.

*Ab initio* calculations of the forces in large supercells are extremely expensive, particularly at lower temperatures, where a large number of beads is required for convergence. To overcome this limitation, we trained a machine learning

interatomic potential (MLIP) exploiting *ab initio* PIMD and MD trajectories generated by some of us in a previous work [1]. In that case, the electronic part was solved within the Becke-Lee-Yang-Parr (BLYP) [5, 6] parametrization of the DFT exchange-correlation functional, as implemented in the Quantum Espresso package [7, 8]. The plain wave cut-off for the energy and for the charge density are set to 90 Ry and 420 Ry, respectively. A  $9 \times 9 \times 9$  reciprocal-space mesh was adopted with a Gaussian Fermi smearing of 0.03 Ry. For training, we used 14640 configurations that span a wide pressure range, from 40 GPa to 220 GPa at both  $T = 100$  K and  $T = 200$  K. Evenly distributed in pressure, about 35 % of them are randomly extracted from PIMD trajectories, the remaining ones are from classical MD. To train the model, we used MACE [9, 10], an equivariant message passing neural network [11, 12] that uses higher-body order messages, resulting in a fast and highly parallelizable model. We used a cutoff radius of 4.0 Å. We tested the performance of the trained MLIP on a test set containing 3660 configuration. In Figs. 1(a) and 1(b), we show the comparison between the predicted and reference energies and forces, respectively. The error distribution is plotted in the insets of the Figures, showing that errors are very small and centered around zero. The resulting mean absolute errors for the energies and forces are 0.363 meV/atom, and 5.25 meV/Å, respectively.

#### FINITE-SIZE SCALING OF THE FERROELECTRIC TRANSITION LINE

In our PIMD simulations, we considered cells containing 32, 108 and 256 atoms corresponding to  $2 \times 2 \times 2$ ,  $3 \times 3 \times 3$  and  $4 \times 4 \times 4$  replicas of the primitive cell, respectively, with periodic boundary conditions. Computing different supercell sizes  $L \times L \times L$  allows us to extrapolate the ferroelectric transition pressure  $p_{\text{QCP}}(L, T)$  for each simulated temperature  $T$ . According to the 4D Ising universality class, the finite-size scaling of the critical coupling is given by[13–15]:

$$p_{\text{QCP}}(L, T) = p_{\text{QCP}}(\infty, T) + \alpha(T)L^{-2} \ln(L)^{-1/6}, \quad (1)$$

at fixed temperature  $T$ . The points  $p_{\text{QCP}}(L, T)$  are plotted in Fig. 2 as a function of  $1/L$  for all the simulated temperatures. The fits based on the functional form in Eq. 1 are also shown. To improve the precision of the fit, we assumed a linear temperature relation of the  $\alpha$  parameter in Eq. 1, such that  $\alpha(T) = \alpha_0 + \alpha_1 T$ . This has been empirically verified from our datapoints taken at  $T = 50$  K, 100 K, 150 K, where the critical pressure for the smallest system  $L = 2$  still falls in the range of validity of the MACE potential. With this model, the reduced  $\chi^2$  of our fits fluctuates around 1. Thus, Eq. 1 captures very well the spatial dependence of the critical couplings. It is another evidence of the validity of the 4D Ising universality class.

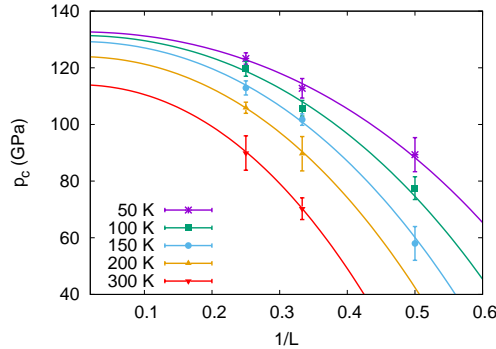


Figure 2. Ferroelectric critical pressures as a function of  $1/L$ , computed at different temperatures, as reported in the legend. The lines are the fitting functions, based on Eq. 1.

The ferroelectric transition line extrapolated to the thermodynamic limit ( $L = \infty$ ) is plotted in Fig. 3, together with the transition lines estimated from our simulations. The error bars on the extrapolated points are computed using the bootstrap method. The transition line for  $L = \infty$  as well the one for  $L = 4$  are also plotted in Fig. 1 of the main paper.

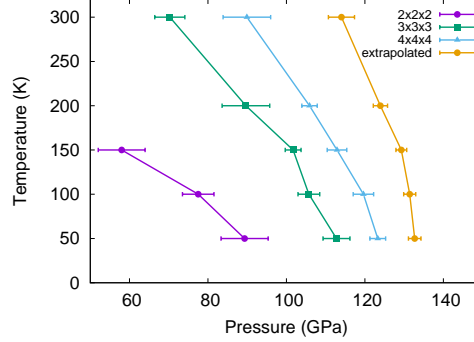


Figure 3. Ferroelectric transition lines computed at different sizes, as reported in the legend. The extrapolated values ( $L = \infty$ ) are obtained from the fit in Fig. 2.

#### CLASSICAL FERROELECTRIC TRANSITION

The classical ferroelectric phase boundaries are computed using the same approach as for the quantum case, namely based on the evaluation of the local parameter and its fluctuations. For classical MD, we carried out simulations for  $L = 4$ , with the aim at performing a direct comparison with PIMD simulations at the same size, the largest attempted in PIMD. The simulation parameters of our classical MD runs are reported in the Methods Section. In Fig. 4(a), we report here the real and absolute value of the order parameter for all the temperatures investigated. As for the quantum case, we locate the ferroelectric transition at the pressure corresponding to the merging of the real and absolute values of the order parameter. In the classical situation, only thermal fluctuations are at play. If they are not strong enough, the protons cannot cross the potential barrier and remain frozen in one of the potential wells, resulting also in a drop of the variance of the order parameter (Fig. 4(b)).

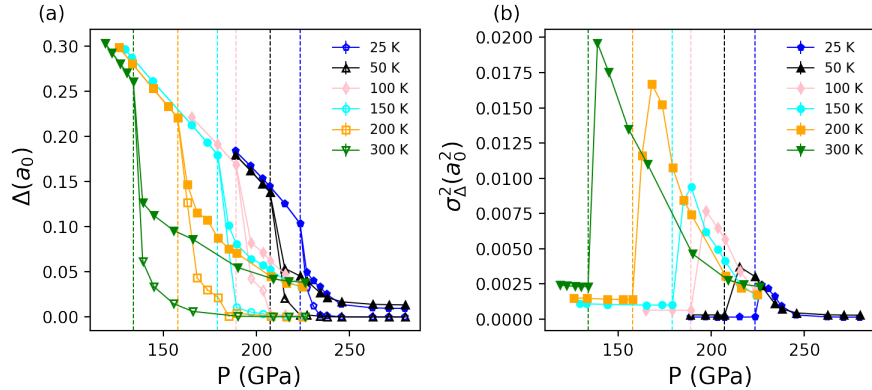


Figure 4. Panel (a): Order parameter for the classical ferroelectric transition. Full and empty symbols indicate the absolute and the real values of the order parameters, respectively. Different temperatures are reported: 25K in blue pentagons, 50K in black triangles, 100K in pink diamonds, 150K in cyan circles, 200K in orange squares and 300K in green reversed triangles. The vertical dashed lines indicate the transition pressures. Panel(b): Variance of the real value of the order parameter of panel (a). Colors and symbols retain the same meaning.

### PROTON DISTRIBUTIONS FROM PIMD AND CLASSICAL MD SIMULATIONS

In Eq. 2 of the main text, we define the local proton displacement, and in Fig. 2(c) of the main paper we plot its distribution along the S-S axis, expressed in crystal units, computed for  $L = 4$  at  $T = 50$  K. Here, we show the distributions of the proton local displacement as computed by PIMD for the same system size at higher temperatures, plotted in Fig. 5. In Fig. 6, we show also the classical distributions, computed by MD for the thermodynamic conditions specified in the plots. Like in the quantum case, from Fig. 6 we can clearly identify the ferroelectric transition, where the unimodal proton distribution is displaced from the S-S midpoint, the unimodal-to-bimodal variation, where the proton distribution acquires a bimodal shape, and finally a unimodal distribution centered in between the S-S distance at even higher pressures.

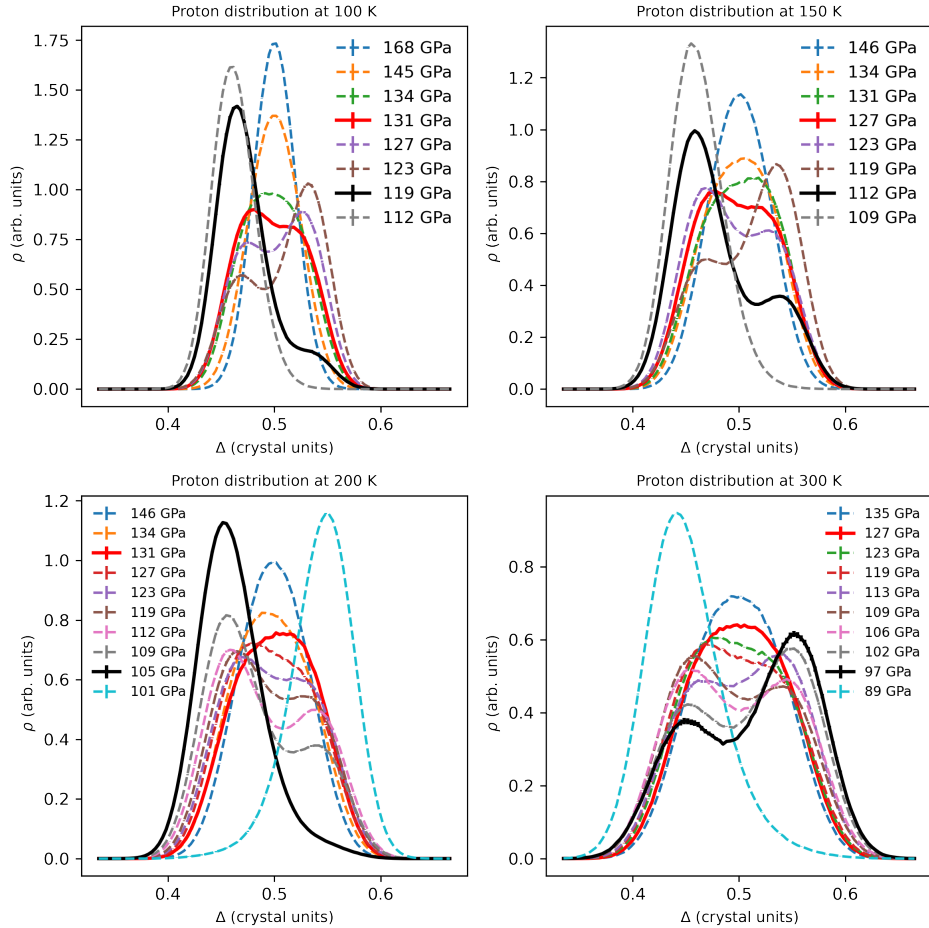


Figure 5. Proton centroid PIMD distributions along the S-S direction for several pressures at  $T = 100$  K, 150 K, 200 K and 300 K. The black and red thick curves correspond to the distributions at the ferroelectric transition and the unimodal-to-bimodal variation, respectively.

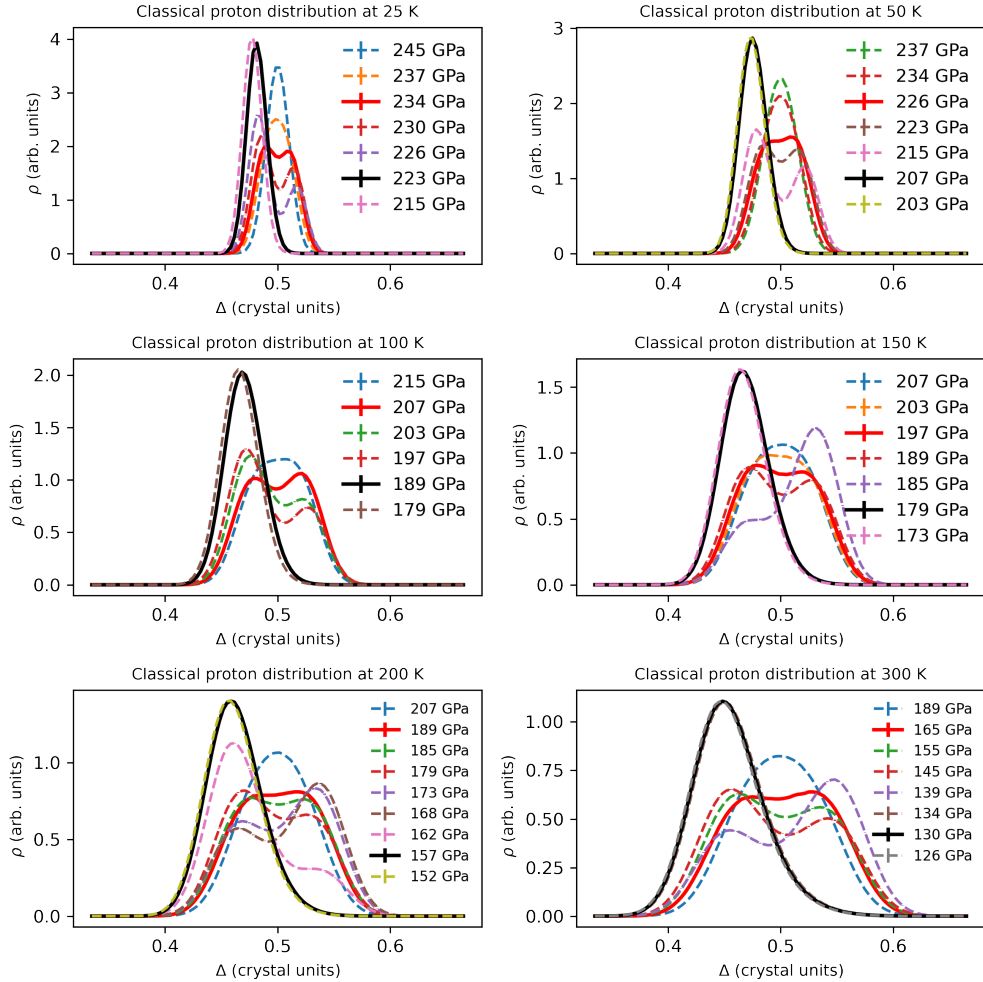


Figure 6. Classical proton MD distributions along the S-S direction for several pressures at  $T = 25$  K, 50 K, 100 K, 200 K and 300 K. The black and red thick curves correspond to the distributions at the ferroelectric transition and the unimodal-to-bimodal variation, respectively.

#### QUANTUM AND CLASSICAL PHASE DIAGRAM

The classical ferroelectric phase boundaries are reported in Fig. 7 as well as in Fig. 1 of the main paper, together with the quantum transition line computed for  $L = 4$ . Compared to the quantum results, the classical ferroelectric transition is shifted to higher pressures. Moreover, the temperature dependence is stronger in the classical case, where there is an increase of about 57 % from room temperature to 50 K, larger than the 36 % increase found in the quantum regime for the same temperature range.

In Fig. 7, we also plot the  $(p, T)$  points where the centered unimodal proton distribution turns into a bimodal shape, signaling the formation of fluctuating local dipole moments, for both quantum and classical simulations. This information is extracted from Fig. 2(c) of the main paper and from Figs. 5 and 6 of the SM. In contrast to the quantum regime, where the unimodal-to-bimodal variation is only marginally affected by temperature, in the classical case we observe a strong temperature dependence. From room temperature down to 50 K, the unimodal-to-bimodal variation

pressure increases by about 40 %.

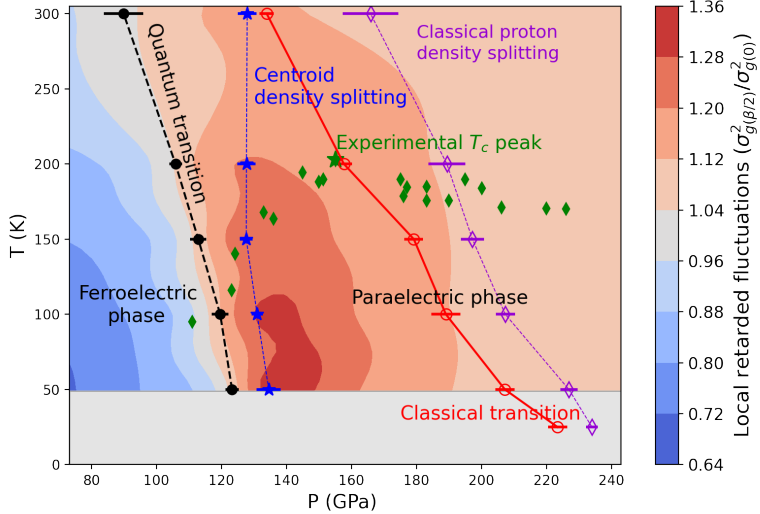


Figure 7. Quantum and classical phase diagram of sulfur hydride for  $L = 4$ . Filled black points and empty red points show the ferroelectric transition lines in quantum and classical simulations, respectively. Blue stars and violet empty diamonds indicate the unimodal-to-bimodal variation in the proton local displacement distribution (density splitting) from PIMD and MD simulations, respectively. Green diamonds are the experimental superconducting temperature, whose peak is shown by a green star[16, 17]. The colormap refers to the  $\sigma_g^2(\beta/2)/\sigma_g^2(0)$  ratio, as defined in the main text; it measures the relative intensity of the retarded fluctuations of local moments. In the dashed gray region, there is no data for interpolation, except for the classical case, where the lowest simulated temperature is 25 K.

#### BEAD AND CENTROID RESOLVED QUANTUM ESTIMATORS

In Fig. 2 of the main paper as well as in Fig. 5, we reported the order parameter and its local distribution along the S-S direction for the centroid positions. It is useful to compare the results obtained when the bead resolution is taken into account and integrated over. In this case, we define the global displacement at the  $j$ -th PIMD iteration as

$$\Delta^{(j)} = \frac{1}{N_H L_\tau} \sum_{i=1}^{N_H} \sum_{k=1}^{L_\tau} [\vec{r}_{H_i S_{i_1}}^{(j,k)} \cdot \hat{r}_{S_{i_1} S_{i_2}}^{(j,k)} - d_{S_{i_1} S_{i_2}}^{(j,k)} / 2], \quad (2)$$

where the  $r_{AB}^{(j,k)}$  vectors connect atom A and B at the  $j$ -th PIMD iteration and for  $k$ -th bead. In principle, the resulting global order parameter may differ from the one computed using the centroid positions. In fact, the projection in Eq. 2 over the versor pointing along the  $S_{i_1}$ - $S_{i_2}$  direction breaks the linear relationship between beads and centroids. To check for possible discrepancies, in Fig. 8 we compare the order parameter as function of pressure at 50 K using the centroid positions and the full bead resolution. It turns out that the choice between beads and centroids has a negligible effect on the estimates of the order parameter, for all pressures explored. The same situation is found for the other temperatures simulated.

While their averages are the same, the distributions differ between bead and centroid resolved estimators. This is apparent from Fig. 9, where we plot the local proton displacement distribution along the S-S direction at  $T = 50$  K and 200 K, to be compared with Fig. 2(c) of the main paper and Fig. 5 of this Supplemental Material (SM), respectively. The distributions computed on the bead positions are broader, owing to the quantum proton delocalization, better captured by the bead resolution. In the bead representation, the unimodal-to-bimodal variation is hidden by the appearance of a shoulder in the bead distribution, instead of a clear peak. Although this variation, and the corresponding local dipole moment formation, can always be detected by a higher-moment analysis of the bead distributions, it is much more transparent in the centroid distributions, which are indeed shown in the main paper.

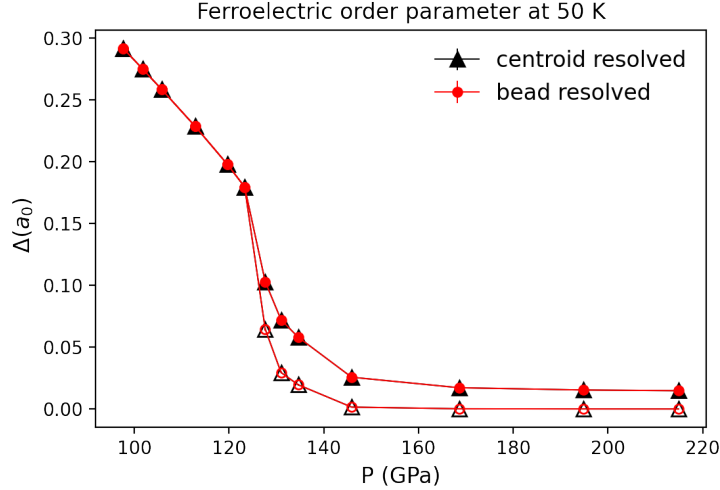


Figure 8. Order parameter at 50 K as a function of pressure. Full and empty symbols correspond to the real values of the order parameter  $\Delta$  and its absolute values  $\Delta_{\text{abs}}$ , respectively. Red (black) color is used to indicate values computed using the centroid positions (the full bead resolution).

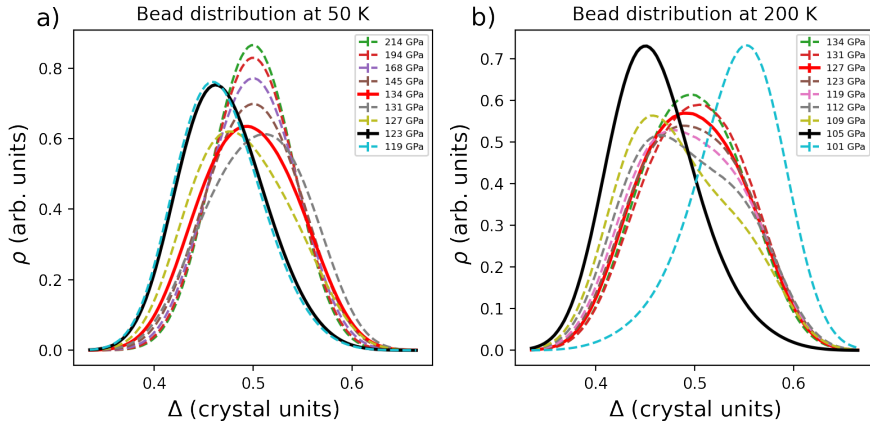


Figure 9. Proton bead distribution along the S-S direction for several pressures. PIMD simulations at 50 K and the 200 K are shown in panel (a) and (b), respectively. The thick red curve corresponds to the pressure where the proton centroid distribution (Fig. 2(c) of the main paper and Fig. 5 of the SM) becomes bimodal and the thick black one plots the distribution at the ferroelectric transition.

#### PIMD PHONONS AND IMAGINARY-TIME RESOLVED PHONON GREEN FUNCTION

We evaluated anharmonic phonon frequencies at the PIMD level by computing the zero-frequency component of the Matsubara Green functions from the quantum displacement-displacement PIMD correlators using the method developed in Refs. [18, 19]. This method relies upon the calculation of the Kubo-transformed displacement-displacement correlators present in the definition of the imaginary-time phonon Green function:

$$G_{ij}(\tau, \mathbf{R}) = -\sqrt{m_i m_j} \langle \mathcal{T} \delta x_i(\tau) \delta x_{j+\mathbf{R}}(0) \rangle, \quad (3)$$

where  $\delta x_i(\tau) = x_i(\tau) - \langle x_i \rangle$  are the atom displacements in the direction  $x$ , as defined in the main text. In Eq. 3,  $\{i, j\}$  run over the atomic indices of the unit cell, while  $\mathbf{R}$  is the index for a Bravais lattice vector contained in the simulation supercell. In PIMD, one can easily compute the imaginary-time averaged displacements  $\delta \tilde{x}_i = \int_0^\beta d\tau \delta x_i(\tau)/\beta$ , with  $\beta = 1/(k_B T)$  the inverse temperature. One can show that the Kubo-transformed phonon Green function  $\tilde{G}_{ij}(\mathbf{R}) = -\beta \sqrt{m_i m_j} \langle \delta \tilde{x}_i \delta \tilde{x}_{j+\mathbf{R}} \rangle$ , computed using the time averaged displacements, is the imaginary-time Fourier transform of Eq. 3 at zero Matsubara frequency ( $i\omega_0 = 0$ ), i.e. the static limit of the phonon Matsubara Green function. Furthermore, by relying on the translational invariance of the system, one can Fourier transform in space the Green function in Eq. 3, and get  $\tilde{G}_{ij}(\mathbf{q})$  on the supercell-allowed  $\mathbf{q}$  vectors. Thus,  $\tilde{G}_{ij}(\mathbf{q}) = G_{ij}(i\omega_0, \mathbf{q})$ . In other words,  $\tilde{\mathbf{G}}(\mathbf{q}) = -\frac{1}{\mathbf{D}(\mathbf{q})^{\text{harm}} + \mathbf{\Pi}(0, \mathbf{q})}$ , where  $\mathbf{D}^{\text{harm}}(\mathbf{q})$  represents the harmonic dynamical matrix of “bare” phonons at the wavevector  $\mathbf{q}$ , and  $\mathbf{\Pi}(0, \mathbf{q})$  is the static limit of the  $\mathbf{q}$ -dependent phonon self-energy  $\mathbf{\Pi}(i\omega_n, \mathbf{q})$ . Therefore, by computing the inverse  $\tilde{\mathbf{G}}^{-1}(\mathbf{q})$ , we have access to the squared phonon frequencies renormalized by static correlations. Indeed,  $\tilde{\mathbf{G}}^{-1}(\mathbf{q})$  enters the associated eigenvalue problem at each  $\mathbf{q}$ :

$$[\langle \delta \tilde{\mathbf{x}} \delta \tilde{\mathbf{x}}^T \rangle_{\mathbf{q}}^{-1}]_{ij} W_{jk}(\mathbf{q}) = m_i \beta \omega_k^2(\mathbf{q}) W_{ik}(\mathbf{q}), \quad (4)$$

where  $\omega_i^2(\mathbf{q})$  is the squared frequency of the  $i$ -th phonon mode at  $\mathbf{q}$ , and  $W_{ji}(\mathbf{q})$  is the eigenvectors matrix. In this work, we therefore solved Eq. 4 after sampling the necessary matrix elements by PIMD, in order to compute the anharmonic phonon branches. We evaluated them on a  $4 \times 4 \times 4$  grid, that has been interpolated to yield the anharmonic phonon dispersion plotted in Fig. 10 for different pressures across the ferromagnetic phase transition at  $T = 200$  K.

To study retardation effects of the one-body phonon Green function in Eq. 3, we also retained the full imaginary-time dependence of the displacement operators  $\delta x_i(\tau)$ , instead of replacing them by their time-averaged version  $\delta \tilde{x}_i$ . In practice, thanks to the imaginary-time periodicity of the phonon Green function, we computed a slightly modified version of Eq. 3, namely

$$G_{ij}(\tau, \mathbf{R}) = -\sqrt{m_i m_j} \langle \mathcal{T} \delta x_i(\tau + \tau') \delta x_{j+\mathbf{R}}(\tau') \rangle \quad \forall \tau', \quad (5)$$

in order to fully exploit the statistics coming from the PIMD samples at different imaginary-time slices. The explicit time dependence in Eq. 5 has been evaluated only for some selected cases, such as the Green function projected on the H local shuttling modes, as explained in the main paper. Indeed, bookkeeping the time dependence is heavier and much more memory demanding than just computing the Kubo-transformed time-integrated PIMD correlation functions.

## 2-BODY PHONON GREEN FUNCTION

Quantum fluctuations in proximity of the ferroelectric QCP manifest themselves not only in the one-body quantities but also in the two-body phonon Green functions. This is even more relevant in the context of “beyond-Migdal” theories of superconductivity, where the exchange of two-phonons is postulated in the electron-phonon coupling. In these theories, the integrated coupling depends on the strength of a local 2-body phonon Green function[20]. Therefore, it is interesting to study how the 2-body phonon Green function evolves across the ferroelectric transition.

As we have seen, PIMD gives access to the quantum imaginary time dynamics. Thus, we would like to study the imaginary-time dependent 2-body phonon Green function  $L(\tau, \tau')$ , defined as:

$$L(\tau, \tau') = \langle \mathcal{T} \delta x(\tau) \delta x(\tau') \delta x(0) \delta x(0) \rangle - \langle \mathcal{T} \delta x(\tau) \delta x(0) \rangle \langle \mathcal{T} \delta x(\tau') \delta x(0) \rangle, \quad (6)$$

where the quantum displacement-displacement correlator  $\langle \mathcal{T} \delta x(\tau) \delta x(0) \rangle$  is proportional to the one-body phonon Green function  $G(\tau)$  in Eqs. 3 and 5, with  $\delta x(\tau)$  the atomic displacement defined above. The 4-point correlators in Eq. 6 can be evaluated from the PIMD sampling as well as the 2-point correlators entering the definition of the one-body phonon Green function. Diagrammatically, Eq. 6 represents the connected, or correlated, part of the two-body phonon Green function, relevant in two-phonon coupling theories. We focus here on the equal-time 2-body phonon Green function, namely  $L_{\text{eq}}(\tau) \equiv L(\tau, \tau)$ , where  $\delta x(\tau)$  is taken for convenience as local proton displacements, defining the local dipole moments in  $\text{H}_3\text{S}$ . To measure the strength of this correlation across the ferroelectric transition, we compute the static limit of  $L_{\text{eq}}(i\omega_n)$ , with  $i\omega_n$  bosonic Matsubara frequencies. This corresponds to  $L_{\text{eq}}(i\omega_0) = \int_0^\beta d\tau L_{\text{eq}}(\tau)$ . We see that  $L_{\text{eq}}(i\omega_0)$  has a magnitude that progressively increases in the paraelectric phase as we move towards lower pressures, by reaching a peak at the ferroelectric transition, before rapidly decreasing at even lower pressures in the ferroelectric

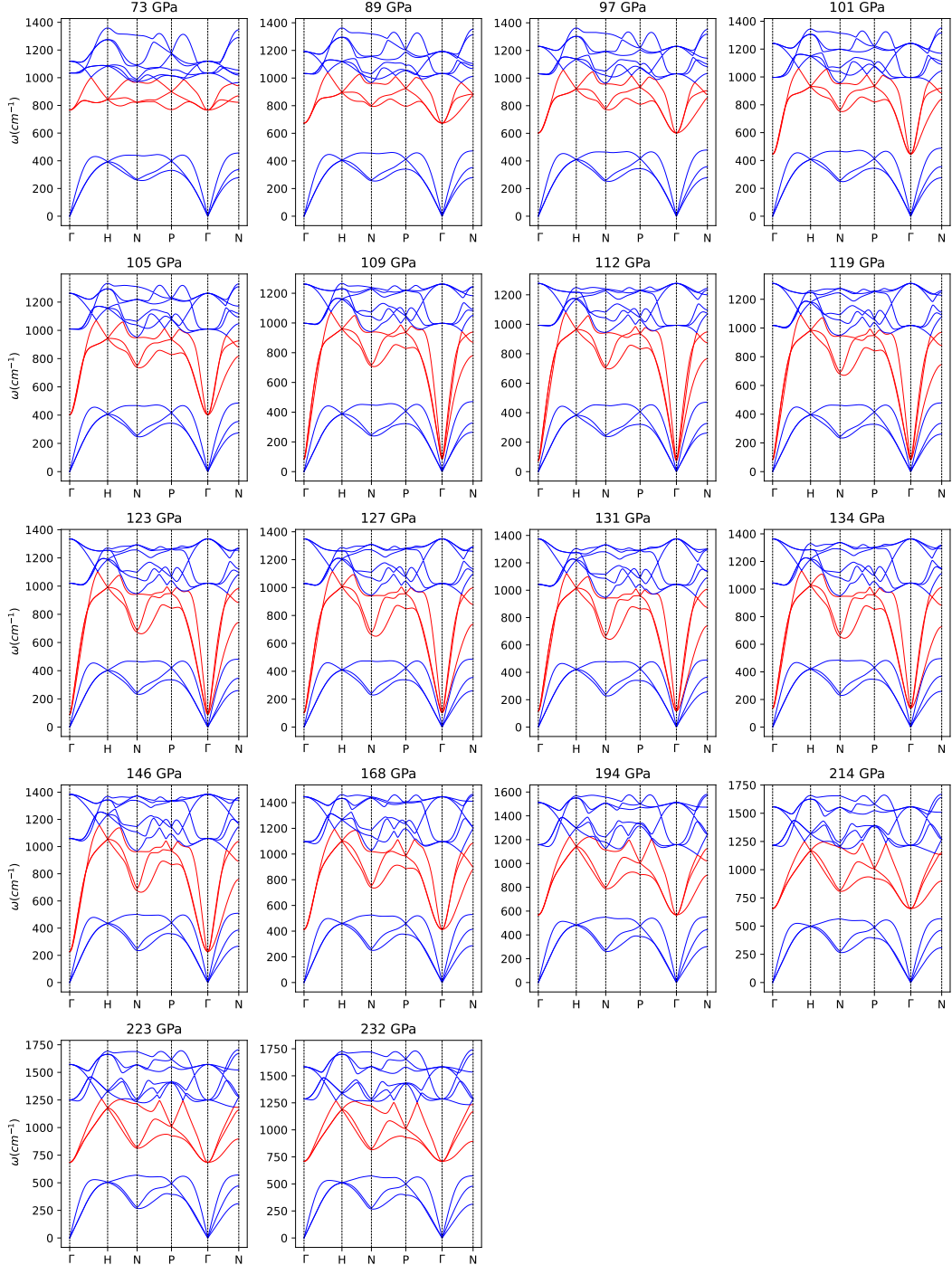


Figure 10. Anharmonic phonon dispersions computed by PIMD simulations at  $T = 200$  K performed in a  $4 \times 4 \times 4$  supercell ( $L = 4$ ), and then interpolated on a finer  $\mathbf{q}$  mesh. Before interpolation, the phonon frequencies  $\omega_i(\mathbf{q})$  and phonon patterns  $W_{ji}(\mathbf{q})$  have been computed by solving Eq. 4 on the supercell-allowed  $\mathbf{q}$  mesh. The branches that soften at the ferroelectric transition are highlighted in red color.

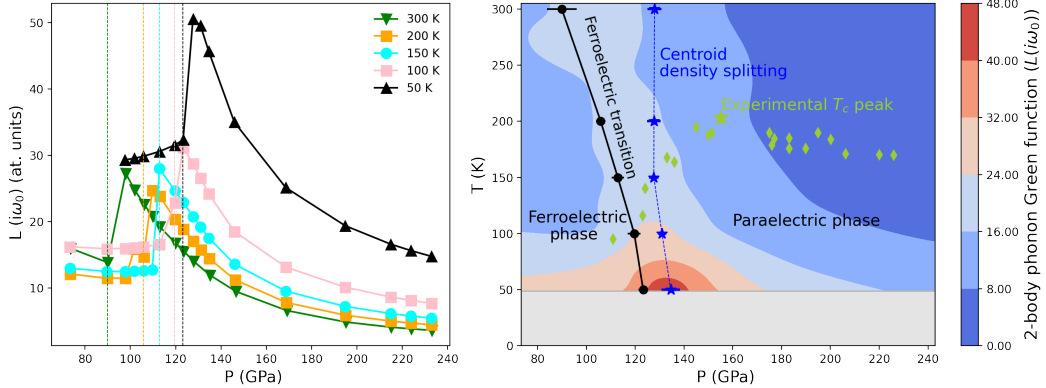


Figure 11. Static limit of the local 2-body phonon Green function  $L_{\text{eq}}(i\omega_0)$  computed by PIMD for  $L = 4$ , for the set of pressures and temperatures represented by the points in panel (a). The displacements in  $L_{\text{eq}}(i\omega_0)$  are the local proton displacements projected on the S-S axis, defining the local dipole moments. Panel (b): heatmap of  $L_{\text{eq}}(i\omega_0)$  in the  $(P, T)$  plane, obtained by a spline interpolation of the points in panel (a) via radially symmetric basis functions. The transition line and the centroid density splitting as determined for  $L = 4$ , together with the experimental  $T_c$  points[16, 17], are also plotted as reference.

phase. Thus, according to our calculations the two-phonon coupling channel could indeed be magnified close to the transition in the paraelectric side.

\* marco.cherubini@sorbonne-universite.fr

† michele.casula@sorbonne-universite.fr

- [1] R. Taureau, M. Cherubini, T. Morresi, and M. Casula, Quantum symmetrization transition in superconducting sulfur hydride from quantum Monte Carlo and path integral molecular dynamics, *npj Computational Materials* **10**, 10.1038/s41524-024-01239-0 (2024).
- [2] M. Ceriotti, M. Parrinello, T. E. Markland, and D. E. Manolopoulos, Efficient stochastic thermostating of path integral molecular dynamics, *The Journal of Chemical Physics* **133**, 10.1063/1.3489925 (2010).
- [3] M. Ceriotti, J. More, and D. E. Manolopoulos, i-PI: A Python interface for ab initio path integral molecular dynamics simulations, *Computer Physics Communications* **185**, 1019–1026 (2014).
- [4] R. Bianco, I. Errea, M. Calandra, and F. Mauri, High-pressure phase diagram of hydrogen and deuterium sulfides from first principles: Structural and vibrational properties including quantum and anharmonic effects, *Phys. Rev. B* **97**, 214101 (2018).
- [5] A. D. Becke, Density-functional exchange-energy approximation with correct asymptotic behavior, *Phys. Rev. A* **38**, 3098 (1988).
- [6] C. Lee, W. Yang, and R. G. Parr, Development of the Colle-Salvetti correlation-energy formula into a functional of the electron density, *Physical review B* **37**, 785 (1988).
- [7] P. Giannozzi, S. Baroni, N. Bonini, M. Calandra, R. Car, C. Cavazzoni, D. Ceresoli, G. L. Chiarotti, M. Cococcioni, I. Dabo, A. Dal Corso, S. de Gironcoli, S. Fabris, G. Fratesi, R. Gebauer, U. Gerstmann, C. Gougaudis, A. Kokalj, M. Lazzeri, L. Martin-Samos, N. Marzari, F. Mauri, R. Mazzarello, S. Paolini, A. Pasquarello, L. Paulatto, C. Sbraccia, S. Scandolo, G. Scalzzeri, A. P. Seitsonen, A. Smogunov, P. Umari, and R. M. Wentzcovitch, QUANTUM ESPRESSO: a modular and open-source software project for quantum simulations of materials, *Journal of Physics: Condensed Matter* **21**, 395502 (2009).
- [8] P. Giannozzi, O. Andreussi, T. Brumme, O. Bunau, M. Buongiorno Nardelli, M. Calandra, R. Car, C. Cavazzoni, D. Ceresoli, M. Cococcioni, N. Colonna, I. Carnimeo, A. Dal Corso, S. de Gironcoli, P. Delugas, R. A. DiStasio, A. Ferretti, A. Floris, G. Fratesi, G. Fugallo, R. Gebauer, U. Gerstmann, F. Giustino, T. Gorni, J. Jia, M. Kawamura, H.-Y. Ko, A. Kokalj, E. Küçükbenli, M. Lazzeri, M. Marsili, N. Marzari, F. Mauri, N. L. Nguyen, H.-V. Nguyen, A. Otero-de-la Roza, L. Paulatto, S. Poncée, D. Rocca, R. Sabatini, B. Santra, M. Schlipf, A. P. Seitsonen, A. Smogunov, I. Timrov, T. Thonhauser, P. Umari, N. Vast, X. Wu, and S. Baroni, Advanced capabilities for materials modelling with Quantum ESPRESSO, *Journal of Physics: Condensed Matter* **29**, 465901 (2017).
- [9] I. Batatia, D. P. Kovacs, G. N. C. Simm, C. Ortner, and G. Csanyi, MACE: Higher Order Equivariant Message Passing Neural Networks for Fast and Accurate Force Fields, in *Advances in Neural Information Processing Systems*, edited by

- A. H. Oh, A. Agarwal, D. Belgrave, and K. Cho (2022).
- [10] I. Batatia, S. Batzner, D. P. Kovács, A. Musaelian, G. N. C. Simm, R. Drautz, C. Ortner, B. Kozinsky, and G. Csányi, The Design Space of E(3)-Equivariant Atom-Centered Interatomic Potentials (2022), arXiv:2205.06643.
- [11] J. Gilmer, S. S. Schoenholz, P. F. Riley, O. Vinyals, and G. E. Dahl, Neural Message Passing for Quantum Chemistry, in *Proceedings of the 34th International Conference on Machine Learning*, Proceedings of Machine Learning Research, Vol. 70, edited by D. Precup and Y. W. Teh (PMLR, 2017) pp. 1263–1272.
- [12] M. M. Bronstein, J. Bruna, T. Cohen, and P. Veličković, Geometric Deep Learning: Grids, Groups, Graphs, Geodesics, and Gauges (2021).
- [13] E. Brézin, An investigation of finite size scaling, *Journal de Physique* **43**, 15 (1982).
- [14] N. Aktekin, The finite-size scaling functions of the four-dimensional Ising model, *Journal of Statistical Physics* **104**, 1397 (2001).
- [15] R. Kenna, Finite size scaling for  $O(N)$   $\varphi 4$ -theory at the upper critical dimension, *Nuclear Physics B* **691**, 292 (2004).
- [16] A. P. Drozdov, M. I. Eremets, I. A. Troyan, V. Ksenofontov, and S. I. Shylin, Conventional superconductivity at 203 kelvin at high pressures in the sulfur hydride system, *Nature* **525**, 73 (2015).
- [17] M. Einaga, M. Sakata, T. Ishikawa, K. Shimizu, M. I. Eremets, A. P. Drozdov, I. A. Troyan, N. Hirao, and Y. Ohishi, Crystal structure of the superconducting phase of sulfur hydride, *Nature Physics* **12**, 835 (2016).
- [18] T. Morresi, L. Paulatto, R. Vuilleumier, and M. Casula, Probing anharmonic phonons by quantum correlators: A path integral approach, *The Journal of Chemical Physics* **154**, 224108 (2021).
- [19] T. Morresi, R. Vuilleumier, and M. Casula, Hydrogen phase-IV characterization by full account of quantum anharmonicity, *Physical Review B* **106**, 054109 (2022).
- [20] D. E. Kiselov and M. V. Feigel'man, Theory of superconductivity due to Ngai's mechanism in lightly doped  $\text{SrTiO}_3$ , *Physical Review B* **104**, 10.1103/physrevb.104.l220506 (2021).